

Measurements of Line Strengths in the $2\nu_1$ Band of the HO₂ Radical Using Laser Photolysis/Continuous Wave Cavity Ring-Down Spectroscopy (cw-CRDS)

Jérôme Thiebaud, Sabine Crunaire, and Christa Fittschen*

Physico-Chimie des Processus de Combustion et de l'Atmosphère (PC2A), CNRS UMR 8522, Université des Sciences et Technologies de Lille, 59655 Villeneuve d'Ascq Cedex, France

Received: January 15, 2007; In Final Form: May 15, 2007

Absolute absorption cross sections of the absorption spectrum of the $2\nu_1$ band of the HO₂ radical in the near-IR region were measured by continuous wave cavity ring-down spectroscopy (cw-CRDS) coupled to laser photolysis in the wavelength range 6604–6696 cm⁻¹ with a resolution better than 0.003 cm⁻¹. Absolute absorption cross sections were obtained by measuring the decay of the HO₂ self-reaction, and they are given for the 100 most intense lines. The most important absorption feature in this wavelength range was found at 6638.20 cm⁻¹, exhibiting an absorption cross section of $\sigma = 2.72 \times 10^{-19}$ cm² at 50 Torr He. Using this absorption line, we obtain a detection limit for the HO₂ radical at 50 Torr of 6.5×10^{10} cm⁻³.

Introduction

The hydroperoxyl radical HO₂ is a key intermediate in low-temperature oxidation processes such as atmospheric chemistry or low-temperature combustion. Because of its importance in both atmospheric and combustion processes, the kinetics^{1–5} as well as the spectroscopy^{6–11} of HO₂ have received intense interest in recent years. The self-reaction of HO₂ is relatively fast,^{5,12,13} and thus, the more important the initial HO₂ concentration is, the faster the self-reaction. Therefore, the techniques used to study the HO₂ radical must present a suitable balance between sensitivity and time resolution. Because it achieves this requirement, UV absorption spectroscopy has become a widely used technique to monitor the HO₂ radical and it has enabled important kinetic data to be acquired.^{13–17} However, the broad and structureless absorption of HO₂ in this wavelength range leads to many overlaps with the absorption features of other species such as peroxy radicals. This lack of selectivity is an important limitation of the UV absorption spectroscopy that encouraged the development of spectroscopic measurements in the infrared region where we can find narrow and resolved absorption lines of small structures such as the HO₂ radical.^{7,9,18–20} Although the mid-infrared range provides stronger absorption cross sections, it induces problems such as line pressure broadening or sampling issues. Peroxy radicals such as HO₂ are known to have absorption bands in the near-IR region, a vibronic progression in the low-lying ${}^2A' \leftarrow {}^2A''$ transition (~ 7017.5 cm⁻¹ for HO₂), as well as the first vibrational overtone in the OH stretch (centered at 6648.9 cm⁻¹ for HO₂). This wavelength range offers weaker line strengths than those in the mid-IR region, but it has other advantages such as less pressure line broadening and the availability of powerful, reliable, and low cost devices (laser sources, detectors, optics, and so forth) from the telecom industry. Therefore, several experiments have been reported using a laser diode in the near-IR to detect HO₂ radicals: DeSain et al.⁶ recorded the HO₂ radical spectrum between 6603.2 and 6685.5 cm⁻¹ using wavelength modulation spectroscopy. This work enabled the assignment of almost 500

lines of the O–H stretching overtone $2\nu_1$ of the HO₂ radical. Christensen et al. monitored HO₂ by the same overtone band at 6638.2 cm⁻¹ to study the kinetics of HO₂ + NO₂²¹ or the HO₂ self-reaction.⁵ Recently, Kanno et al. measured the nitrogen and water-pressure broadening coefficients of the HO₂ band at ~ 7020.8 cm⁻¹ (ref 22) and the rate enhancement effect of water on HO₂ self-reaction¹² using two-tone frequency modulation (TTFM) absorption spectroscopy.

We recently introduced a new way to perform time-resolved detection of the HO₂ radical in a photolysis reactor by using continuous wave cavity ring-down spectroscopy (cw-CRDS) in the near-IR.²³ We recorded HO₂ absorption lines and self-reaction kinetics with a 10 μ s time resolution and a detection limit of 2×10^{12} molecules cm².

The increasing number of papers using the near-IR shows that this spectral region is convenient for the detection of HO₂ radicals. Nevertheless, the absorption line strengths of the HO₂ radical in this spectral region are not well-known. In Figure 1 are illustrated all published absorption cross sections, calculated to Doppler limiting conditions for comparison, along with values obtained in this work in the same wavelength range. In 1991, Johnson et al. published the first line strengths of the HO₂ radical in this wavelength range.⁹ They measured 23 lines by two-tone frequency modulation spectroscopy (TTFMS) at ~ 1509 nm (with an accuracy of approximately 0.5 nm) and calibrated the HO₂ concentration by modulated-photolysis UV absorption spectroscopy; they found peak absorption cross sections of $\sigma = 1–10 \times 10^{-20}$ cm². However, they mentioned several error sources: uncertainties in the TTFMS calibration, changes of HO₂ concentration due to instabilities in pressure and photolysis rates during the course of the experiment, and changes in the diode laser output power I_0 . They estimated the accuracy of the absorption cross sections to be $\sim 50\%$. In 1997, Taatjes and Oh²⁴ published as a foot note the line strength of the line at 6625.8 cm⁻¹ to be $S = 2.4 \times 10^{-21}$ cm² molecule⁻¹ cm⁻¹, stating that the manuscript is in preparation; no details on how this line strength was obtained were given. Recently, Christensen et al.²¹ have estimated the peak cross section of the transition at 6638.2 cm⁻¹ to be $\sigma = (4 \pm 2) \times 10^{-20}$ cm² in 100 Torr N₂: this cross section was determined by comparison to the HO₂

* To whom correspondence should be addressed. Fax: +33 3 20 33 72 66. E-mail: christa.fittschen@univ-lille1.fr.

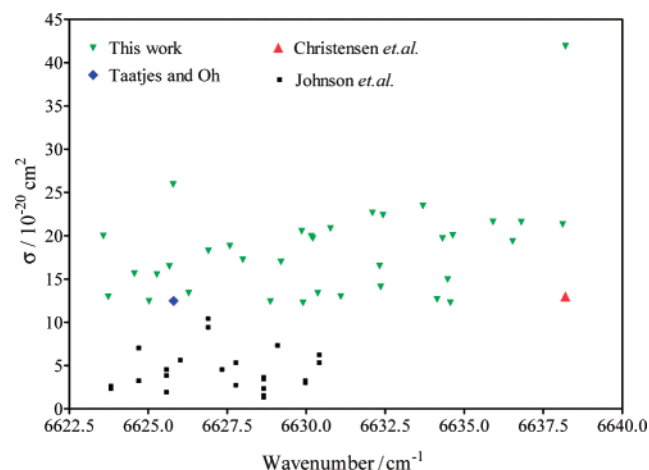


Figure 1. Comparison of absorption cross sections from this work with available literature values: Christensen et al.,²¹ Taatjes and Oh,²⁴ and Johnson et al.⁹

TABLE 1: Characteristics of the Experimental Setup for Spectroscopic and Kinetic Measurements^a

	spectroscopy	kinetic
precursor	SOCl ₂	Cl ₂
IR laser source	Agilent laser module	DFB laser
mirrors	Layertec	Los Gatos
<i>R</i>	0.99974	0.99996
<i>L_A</i> /cm	30	37
α_{\min} /cm ⁻¹ Hz ^{-1/2}	2×10^{-8}	1.2×10^{-9}
[HO ₂] _{min} /cm ⁻³	1.5×10^{12b}	6.5×10^{10b}

^a *R*: reflectivity of the cavity mirrors; *L_A*: overlap length between photolysis and detection volume; α_{\min} : absorption coefficient noise equivalent, and [HO₂]_{min}: HO₂ concentration noise equivalent for $\sigma = 2.72 \times 10^{-19}$ cm². ^b [HO₂]_{min} was lower than expected from α_{\min} due to strong absorption of CH₃OH and thus lower τ_0

cross sections of the transitions near 6627 cm⁻¹ obtained by Johnson et al. in 1991.

While the line positions of the overtone $2\nu_1$ transition of the HO₂ radical have been carefully measured and assigned by DeSain et al.,⁶ there is clearly a need for more reliable absolute absorption cross sections of the HO₂ radical. In the present paper, we therefore report our results on the measurement of the line strength of the high resolution absorption spectrum in the O–H stretching overtone $2\nu_1$ band by cw-CRDS coupled to laser photolysis. We have used the HO₂ self-reaction kinetics to extract the absorption cross section at a given wavelength and pressure for eight lines exhibiting a large range of line strength. From these measurements was extracted a calibration factor permitting calibration of the entire spectrum previously recorded.

Experimental Setup

The experimental setup is described in detail in ref 23. Major improvements have been accomplished since (summarized in Table 1) and have been beneficial to the calibration of the spectrum. The experimental setup comprises three main components: the quasi-static reactor, the photolysis excimer laser (Lambda Physic LPX 202i), and the cw-CRD spectrometer (see Figure 2).

A stainless steel flow cell was used as a chemical reactor to enable the implementation of the cw-CRD spectrometer (cavity length 78 cm). The overlap between the probe laser beam and the photolysis laser beam was maximized to obtain the highest sensitivity, that is, the IR-beam crosses the photolysis beam at an angle of 4° (Figure 2). The length of the overlap region *L_A*

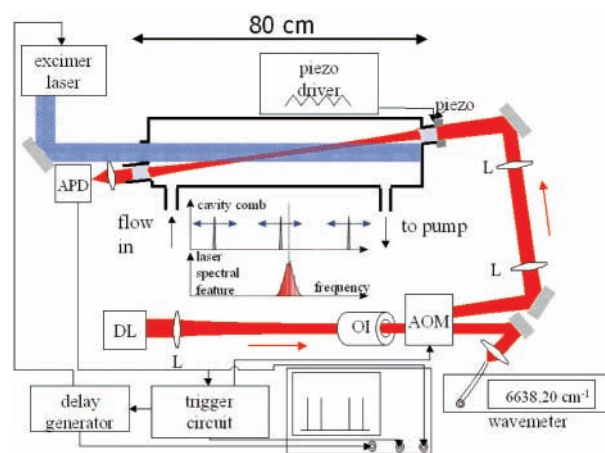
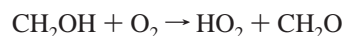
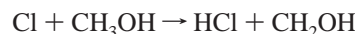


Figure 2. Schematic of the experimental setup. DL: diode laser; OI: optical isolator; AOM: acousto-optical modulator; APD: avalanche photodiode; and L: lens.

was calculated from geometrical basics, and it was 30 cm for measuring the absorption spectrum and was increased to 37 cm for the kinetic measurements by guiding the photolysis beam with a 1 inch dielectrical mirror instead of a 2 cm quartz prism. HO₂ radicals were prepared by the following reaction sequence



Cl atoms were generated via laser photolysis of two different precursors: SOCl₂ at 248 nm and Cl₂ at 351 nm. SOCl₂ was used for measuring the absorption spectrum, because the excimer laser was set to work at 248 nm and SOCl₂ is known to be an efficient precursor for Cl atoms at this wavelength.²⁵ The reactant concentrations for recording the entire spectrum were O₂ = 3.3×10^{16} cm⁻³, CH₃OH = 1.1×10^{16} cm⁻³, and SOCl₂ = 2.6×10^{14} cm⁻³, leading with a photolysis energy of 300 mJ/pulse to an estimated initial HO₂ concentration of 1.3×10^{14} cm⁻³.

As already mentioned in our previous paper,²³ the chemistry of the SOCl radicals under our conditions is not known and may influence the HO₂ concentration time profile. This will have no influence on the recording of the spectrum, since for each wavelength the signal is acquired using the same experimental conditions and averaging eight data points within the same time segment (0–2 ms after the photolysis pulse). However, the calibration of this spectrum was obtained through measuring HO₂ decays, and this requires accurate knowledge of the HO₂ loss processes. We have therefore switched the excimer laser wavelength to 351 nm to be able to photolyze Cl₂, which is well-known to be a clean source of Cl atoms. HO₂ decays using Cl₂ as a precursor were measured at variable concentrations between 1×10^{15} cm⁻³ and 5×10^{16} cm⁻³ Cl₂, leading to estimated initial HO₂ concentrations of $1\text{--}10 \times 10^{13}$ cm⁻³. The absorption spectrum was measured at a total pressure of 50 Torr He, and kinetic decays were measured in the pressure range 20–100 Torr. Typical total gas flows were 700 cm³ min⁻¹ at 50 Torr, leading to a flow velocity within the reactor of 7 cm s⁻¹. The different gases were introduced into the cavity as stabilized flows using calibrated flow controllers (Tylan FC-260). The total pressure was kept constant using the pressure controller (Leybold-Heraeus MR 16) installed at the exit of the reactor. Experiments were performed at a photolysis repetition rate of 0.5 Hz, permitting a sufficient renewal of the reaction mixture between two photolysis laser shots. The temperature of the gas mixtures was 296 ± 3 K.

The near-infrared beam was provided by two different laser sources: a fibered tunable laser module (Agilent 81680A) for acquisition of the absorption spectrum and a fibered distributed feedback (DFB) diode laser (Fitel-Furukawa) for the kinetic measurements. The Agilent laser module is mode hop-free tunable from 1460 to 1580 nm, allowing scanning of the HO₂ absorption feature over a large wavelength range. Its technical specifications indicate a ± 5 pm relative wavelength accuracy and a ± 0.01 nm absolute accuracy. We measured at the fibered output a power of $180 \mu\text{W}$ at 1460 nm increasing to a maximum of 1.6 mW at 1570 nm. The DFB diode laser allows working with much higher power (until 20 mW) but only within a small wavelength range for the diode used in this work at $\sim 1506 \pm 3$ nm.

The radiation is coupled into the cavity through a set of lenses and mirrors to obtain a good cavity mode match to excite the fundamental TEM₀₀ mode. The beam passes through an optical isolator and an acoustooptical modulator, allowing deviation of the laser beam within 350 ns with respect to the trigger signal. In addition to the Agilent laser controller, the diode laser emission wavelength was monitored using a fibered wavemeter (Burleigh WA-1100) with an accuracy of 0.01 cm^{-1} . A good agreement, except for a systematic shift of 0.056 cm^{-1} , was found between these two sources; thus, no additional wave-number calibration was performed. The optical signal transmitted through the cavity is converted into current by an avalanche effect photodiode (Perkin-Elmer C30662E). A homemade amplifier-threshold circuit converts the current signal to an exploitable voltage signal and triggers the acquisition, that is, the acoustooptical modulator, the delay generator (PAR 9650), and the digital oscilloscope (Tektronix TDS5052) that is used for data recording. The entire detection system has a bandwidth of 5 MHz. A personal computer is connected to the main devices either by GPIB or via a digital/analogic acquisition card (National Instruments PCI-6221). Control of the experiment and data acquisition and processing were executed by LabVIEW 7.1 virtual instruments.

To extract the ring-down times, the trigger signal and the output from the avalanche photodiode are recorded by the oscilloscope with 200 ns time resolution during 20 ms for spectroscopic measurements and 40 ms for kinetic measurements. Since HO₂ has a short lifetime limited by its rapid self-reaction, recording its spectrum requires detecting it shortly after the photolysis pulse to obtain a strong absorption signal. To acquire both the zero absorption baseline and the HO₂ absorption signal, recording is started 18 ms before the photolysis pulse, permitting one (or more) ring-down event(s) before the photolysis pulse and, in general, another one within 2 ms after the photolysis flash to be obtained. For measuring the kinetic decay of the radical concentration, recording is started 4 ms before the photolysis pulse, permitting one (sometimes two) ring-down event(s) before the photolysis pulse and several (two–six in general) ring-down events after the photolysis pulse to be obtained. After entirely transferring both traces to the computer, the positions of the individual ring-down events, and thus the delay with respect to the photolysis pulse, are first extracted from the trigger signal trace, and the individual cavity ring-down decays are then sampled into a $160 \mu\text{s}$ time window for the spectroscopic measurements and a $320 \mu\text{s}$ time window for the kinetic experiments, starting at each trigger signal. The ring-down time is then roughly estimated by linear regression of the logarithmic decay and thereafter fitted over 4 lifetimes by a Levenberg–Marquardt LabVIEW virtual instrument. Two different sets of mirrors were used: mirrors with $R = 99.974\%$

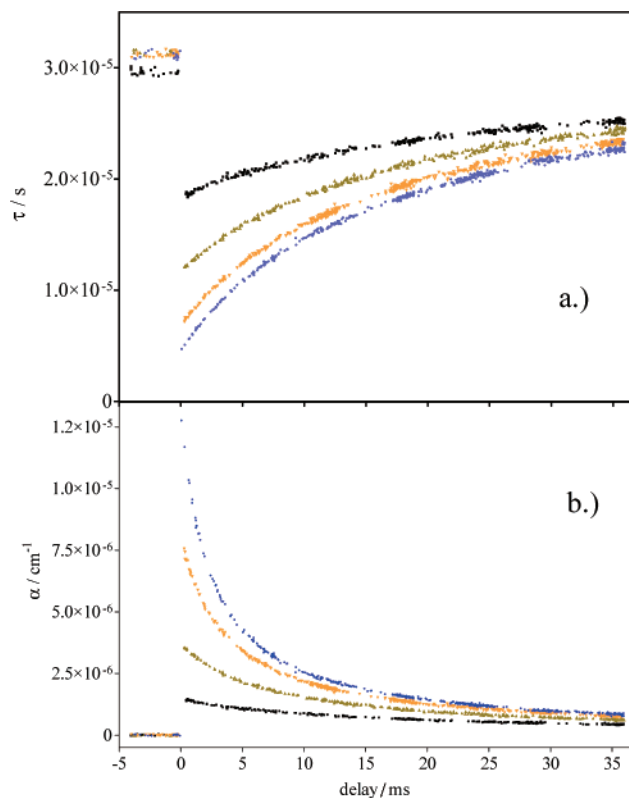


Figure 3. Kinetic measurements at 6640.31 cm^{-1} for four initial Cl₂ concentrations: 1.25×10^{15} , 2.7×10^{15} , 5.6×10^{15} , and 10×10^{15} molecules cm^{-3} from top to bottom in the upper graph. (a) Ring-down time τ plotted as a function of the delay relative to the photolysis pulse. (b) Absorption coefficient α plotted as a function of the delay relative to the photolysis pulse.

(Layertec) leading to typical decay times in the empty cavity of $10 \mu\text{s}$ for the spectroscopic measurements and mirrors with $R = 99.9956\%$ (Los Gatos) leading to typical decay times in the empty cell of $60 \mu\text{s}$ for the calibration measurements.

For measuring the absorption spectrum (see Figures 8 and 9 and the Supporting Information), typically eight events occurring after the photolysis pulse are averaged, requiring in general eight photolysis pulses (i.e., 16 s) before increasing the laser wavelength by 0.0022 cm^{-1} (or $5 \times 10^{-4} \text{ nm}$) for the next sequence of recordings. Using this method, the overall scan speed is $\sim 0.6 \text{ cm}^{-1} \text{ h}^{-1}$. For measuring kinetic decay (see Figure 3), ~ 400 ring-down events are typically sampled, leading to a typical recording time of less than 10 min. Table 1 summarizes the characteristics of the experimental setup for the kinetic and spectroscopic measurements.

Results and Discussion

The ring-down time τ is extracted from the signal through

$$I(t) = I_0 \exp\left(-\frac{t}{\tau}\right) \quad (1)$$

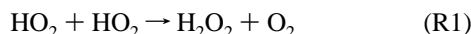
where $I(t)$ and I_0 are the signals transmitted by the cavity. Typical signals, as obtained with our experimental setup, are shown in Figure 3a for different precursor concentrations: the ring-down time is measured relative to the photolysis pulse (occurring at $t = 0 \text{ ms}$), each dot represents one ring-down event, and no averaging was performed. As shown in Figure 3b, the absorption coefficient α , at a given delay can be calculated from the decay time τ_0 of the empty cavity (in our case, before the photolysis pulse, i.e., $t < 0 \text{ ms}$) and the decay time τ_t of the

cavity containing the sample (i.e., after the photolysis pulse, $t > 0$ ms):

$$\alpha_t = [A]_t \sigma = \frac{R_L}{c} \left(\frac{1}{\tau_t} - \frac{1}{\tau_0} \right) \quad (2)$$

where R_L is the ratio between cavity length L (distance between the two cavity mirrors) and length L_A over which the absorbing species is present (in our case, the overlap between the photolysis beam and absorption path) and c is the light speed. One can extract either the absorption cross section σ for spectroscopic measurements or the concentration $[A]_t$ of the target molecule for kinetic experiments. While the kinetic of reaction (R1) has been the subject of many investigations, mainly by UV absorption spectroscopy,^{8,26–30} quantitative information on the near-infrared spectroscopy of the HO₂ radical is sparse.⁹ We have therefore reversed the procedure and have deduced the initial HO₂ radical concentration and thus the absorption cross section σ from the time-resolved absorption profiles.

Kinetic Measurements. Under our experimental conditions, the decay of HO₂ concentration, as shown in Figure 3b, results mainly from the well-studied self-reaction^{5,12,13,31,32}



and, less importantly, through diffusion out of the photolysis volume



Approximating the diffusion process to an exponential loss, the HO₂ concentration–time profile is governed by the rate constants k_1 and k_{diff} :

$$\frac{d[\text{HO}_2]}{dt} = -2k_1[\text{HO}_2]^2 - k_{\text{diff}}[\text{HO}_2] \quad (3)$$

Under reaction conditions where (R1) is the major loss process, that is, at short reaction times, the decay can be approximated to the linear equation

$$\frac{1}{[\text{HO}_2]_t} = \frac{1}{[\text{HO}_2]_0} + \left(\frac{k_{\text{diff}}}{[\text{HO}_2]_0} + 2k_1 \right) t \quad (4)$$

with $[\text{HO}_2]_t$ being the radical concentration at time t and $[\text{HO}_2]_0$ being the initial radical concentration. A plot of $1/[\text{HO}_2]_t = f(t)$ results then in a straight line with a slope corresponding to $k_{\text{diff}}/[\text{HO}_2]_0 + 2k_1$ and an intercept of $1/[\text{HO}_2]_0$. Measuring the kinetic decays for several $[\text{HO}_2]_0$ concentrations permits therefore distinguishing between diffusion and self-reaction.

A plot of

$$\frac{1}{\alpha} = \frac{1}{[\text{HO}_2]_t \sigma_\lambda} = f(t) \quad (5)$$

leads to a straight line with a slope of $m = k_{\text{diff}}/[\text{HO}_2]_0 \sigma_\lambda + 2k_1/\sigma_\lambda$ and an intercept of $I = 1/[\text{HO}_2]_0 \sigma_\lambda$. Figure 4 shows such a plot for three different absorption lines with absorption cross sections between 0.32 and $1.2 \times 10^{-19} \text{ cm}^{-1}$. Using the same initial HO₂ concentration, the influence of the absorption coefficient σ on the slope and intercept is clearly visible. Figure 5 shows the same plot ($1/\alpha = f(t)$) for the signals from Figure 3b: the straight line represents the linear regression of all data between 0 and 5 ms, as shown in the inset. The linearity in this time frame is very good for all concentrations, but one can

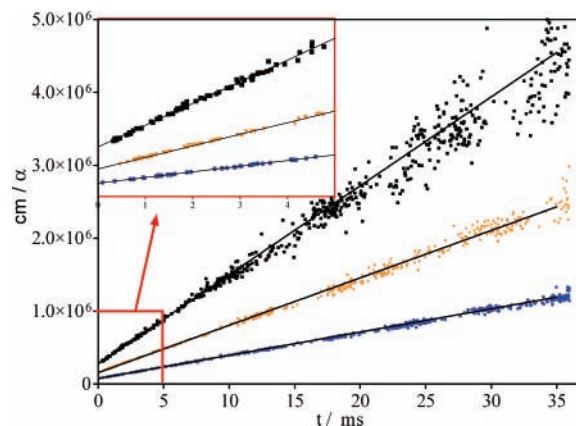


Figure 4. Plot of $1/\alpha = f(t)$ for three different absorption lines using the same concentration of $\text{Cl}_2 = 1 \times 10^{16} \text{ molecules cm}^{-3}$: 6637.45, 6640.98, and 6640.31 cm^{-1} with absorption cross sections of 3.15×10^{-20} , 5.92×10^{-20} , and $11.5 \times 10^{-20} \text{ cm}^2$, respectively, from top to bottom. The straight lines show the linear regression for the experimental data between 0 and 5 ms, and the inset shows a magnified view of this section.

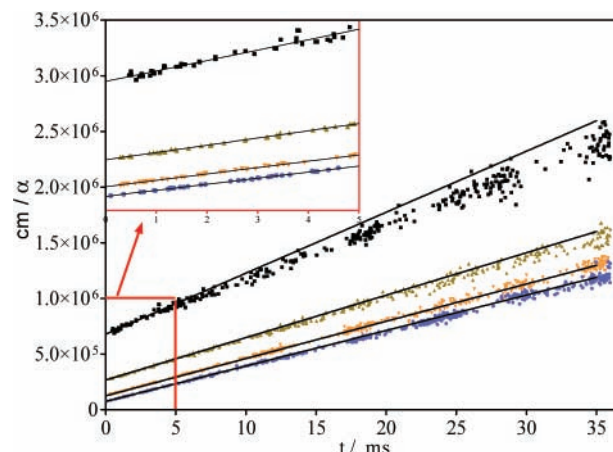


Figure 5. Plot of $1/\alpha = f(t)$ for the signals from Figure 3b. The straight lines show the linear regression for the experimental data between 0 and 5 ms, and the inset shows a magnified view of this section.

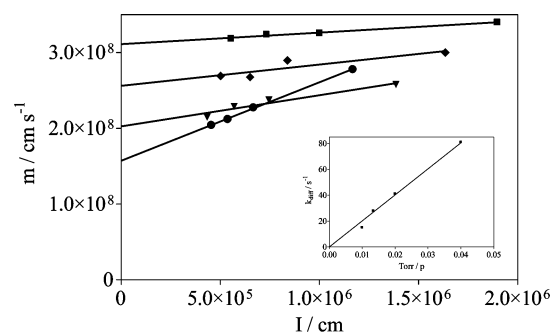


Figure 6. Plot of the slope m as a function of the intercept I from Figure 4- and 5-type plots at four different pressures (25, 50, 75, and 100 Torr from bottom to top, respectively) and four different initial Cl_2 concentrations at each pressure obtained at 6637.29 cm^{-1} . The inset shows the slopes of the regressions as a function of $1/p$.

observe a deviation from linearity toward long reaction times and low concentrations; that is, the approximation in eq 4 is not valid anymore. The slight increase in the initial slope m with decreasing initial HO₂ concentration is a result of the diffusion loss (R2); this loss becomes more important relative to (R1) with decreasing initial HO₂ concentration. Figure 6 illustrates the influence of diffusion: the slope m is plotted as a function of the intercept I for four initial HO₂ concentrations

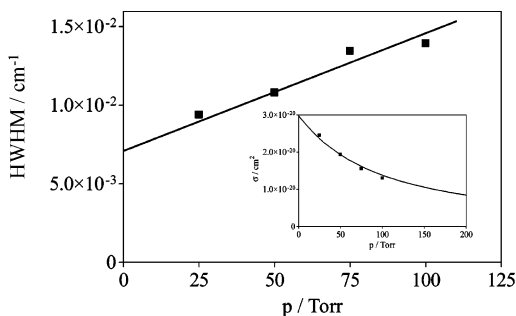


Figure 7. Plot of the pressure broadening coefficient γ_{coll} , obtained from a Voigt fit of the entire absorption line at 6637.29 cm^{-1} . The inset shows the absorption cross section σ , obtained from kinetic decays, as a function of pressure.

at four different pressures between 25 and 100 Torr. The unimolecular rate constant k_{diff} is directly obtained from the slope of these plots and is reported in the inset of Figure 6 as a function of $1/p$ for the four pressures. The correlation is very good, which strongly supports our assumption that the increase in the slope with decreasing initial HO₂ concentration is due to diffusion. The absorption coefficients used for the calibration of the absorption spectrum (see next section) have therefore been deduced from measurements of kinetic decays for several initial radical concentrations and extrapolation of eq 5 to infinite [HO₂]₀, that is, the intercept $I = 2k_1/\sigma_2$ of Figure 6-type plots.

The rate constant k_1 is known to be enhanced by molecules such as H₂O, CH₃OH, or NH₃,^{3,12,13,29,31,33,34} but the concentrations used in this work are too low to become important. According to Stone and Rowley,¹³ a CH₃OH concentration of 10^{16} cm^{-3} leads at 296 K to an enhancement of the rate constant of $4.2 \times 10^{-16} \text{ cm}^3 \text{ s}^{-1}$. Recently, Christensen et al.³ have reported the thermodynamics and kinetics of the HO₂·CH₃OH complex formation as well as the rate constant for the reaction of the addition complex with HO₂ and argued for a reinterpretation of the experimental results of Stone and Rowley. Nevertheless, extrapolation of the equilibrium constant to our temperature and CH₃OH concentration shows that ~1% of the HO₂ is trapped in the addition complex, with the addition complex reacting ~10 times faster than HO₂ itself. As a consequence, we consider that under our conditions we can safely neglect any enhancement of the rate constant and have therefore adopted the average of the latest recommendations of IUPAC³⁵ and NASA:³⁶ $k_1 = 1.65 \times 10^{-12} + 4 \times 10^{-32}[\text{He}] \text{ cm}^3 \text{ s}^{-1}$.

The decrease of the absorption coefficient with increasing pressure, due to pressure broadening of the absorption line, is greatly visible in Figure 6: the intercept and thus the absorption coefficient decrease by nearly a factor of 2 from 2.5 to $1.3 \times 10^{-20} \text{ cm}^2$ with a pressure increase from 25 to 100 Torr He, as shown in the inset of Figure 7. The absorption line at 6637.29 cm^{-1} was measured for all four pressures, and each line was fitted to a Voigt profile using the theoretical Doppler half width of $7.09 \times 10^{-3} \text{ cm}^{-1}$. The obtained half widths at half-maximum (HWHM) are plotted as a function of pressure in Figure 7, and they lead to a broadening coefficient of $0.057 \text{ cm}^{-1} \text{ atm}^{-1} \text{ He}$. This value can be compared to those from recent measurements of the broadening coefficient of other bath gases: Kanno et al.²² obtained γ_{coll} values of 0.101 and $0.216 \text{ cm}^{-1} \text{ atm}^{-1} \text{ N}_2$ and H₂O, respectively, and we have obtained recently³⁷ values between 0.078 and $0.155 \text{ cm}^{-1} \text{ atm}^{-1}$ for air-broadening, depending on the rotational quantum number. These values are significantly higher, which is in good agreement with the expected large difference in collision efficiency between He and the other bath gases. The full line in the inset of Figure 7 shows

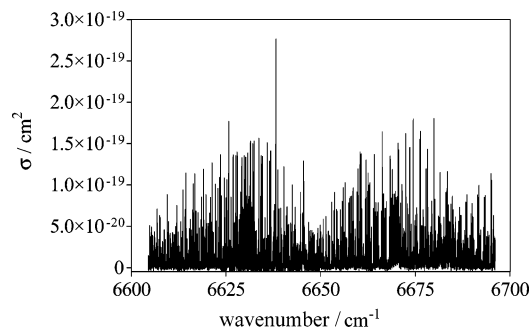


Figure 8. HO₂ absorption spectrum in the range $6604.5\text{--}6696 \text{ cm}^{-1}$ at 50 Torr.

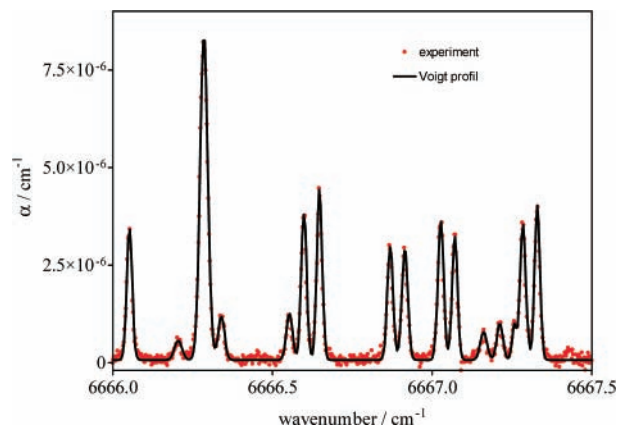


Figure 9. Portion of the absorption spectrum from Figure 8 between 6666.0 and 6667.5 cm^{-1} : the full line shows the fit of a Voigt profile to the experimental data.

a simulation of the absorption cross section at the line center of a Voigt profile as a function of pressure using $\gamma_{\text{coll}} = 0.057 \text{ cm}^{-1}$ and an integrated line strength of $S = 4.5 \times 10^{-22} \text{ cm}^2 \text{ molecule}^{-1} \text{ cm}^{-1}$, which is the average value obtained from the integration of the entire line profile for all four pressures after normalizing. Note the good agreement between the pressure broadenings obtained by two different methods: (i) by scanning the full absorption line and (ii) by deducing the absorption cross section at the line center wavelength from time-resolved decays.

Absorption Spectrum. The absorption spectrum of the HO₂ radical was measured at a total pressure of 50 Torr He in the range of $6604\text{--}6696 \text{ cm}^{-1}$ using the Agilent diode laser source. In this wavelength range, more than 40 000 data were measured with a resolution better than 0.003 cm^{-1} , with each data being the average of eight ring-down events occurring within 2 ms after the photolysis pulse, obtained at a repetition rate of 0.5 Hz. The entire spectrum is shown in Figure 8, where more than 900 lines have been detected in this wavelength range. A magnified view of the entire spectrum is available as Supporting Information; the positions of the 491 lines assigned by DeSain et al.⁶ to the 2ν₁ band of the HO₂ radical are shown as dots. A very good agreement for most of the line positions was found.

All peaks of the spectrum have been fitted to a Voigt profile; an example of such a fit is shown in Figure 9. The absorption coefficients α obtained from these fits were brought to an absolute scale by the following calibrating procedure: the absorption cross sections σ of eight absorption lines chosen within the range accessible with the DFB diode, exhibiting a wide range of line strengths and being relatively isolated from other lines, were determined at 50 Torr from kinetic decays as described in the above paragraph; that is, the kinetic decays were measured with different initial precursor concentrations and the absorption cross section σ was extracted from the

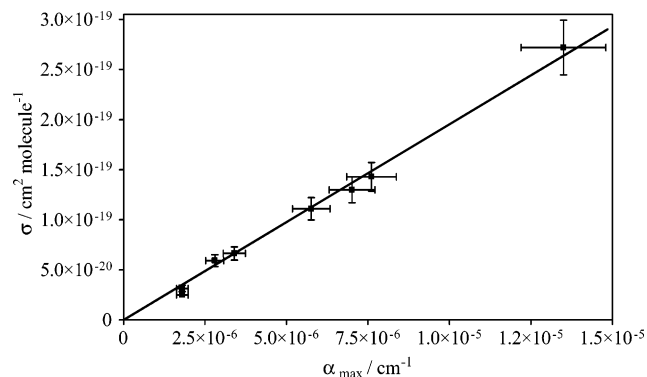


Figure 10. Plot of absorption cross sections σ , obtained from kinetic decays, as a function of the peak height, obtained from a Voigt fit of the absorption spectrum at 50 Torr for eight absorption lines in the wavelength range 6633–6641 cm^{-1} . The error bars represent an estimated experimental error of 10%.

TABLE 2: Absorption Cross Section for the Eight Distinct Absorption Lines Used for Calibration of the Entire Spectrum. All Cross Sections Are Obtained from Measurements of the Kinetic Decays at Various Precursor Concentrations

ν/cm^{-1}	$\sigma_{50 \text{ Torr}}/(10^{-19} \text{ cm}^2)$
6633.70	1.43
6635.92	1.30
6637.46	0.32
6637.73	0.66
6638.20	2.72
6638.58	0.25
6640.31	1.11
6640.98	0.59

intercept of Figure 6-type plots. The absorption cross sections for all eight lines obtained in this way are given in Table 2. Figure 10 shows the plot of these absorption cross sections σ as a function of the absorption coefficients α obtained from the Voigt profile fit; a very good correlation was obtained. The absorption coefficients α from all lines of the entire spectrum were then converted to absorption cross sections σ using the calibration factor obtained in Figure 10. Table 3 summarizes, for the 100 most intense lines, the center wavelength, the absorption cross section σ , and the full width at half-maximum (FWHM). As can be seen from Figure 8, the absorption line at 6638.20 cm^{-1} surpasses all other lines by nearly a factor of 2, and the absorption cross section at 50 Torr was determined to be $\sigma = 2.72 \times 10^{-19} \text{ cm}^2$ for this line. Very likely, this absorption line represents the convolution of two lines, but even at low pressure no deconvolution could be observed.

The absorption cross sections can be compared to the few available data in the literature (all existing data are in the wavelength range 6623–6639 cm^{-1} ; see Figure 1): Johnson et al.⁹ reported maximal line strengths of $S = 1.6 \times 10^{-21} \text{ cm}^2 \text{ molecule}^{-1} \text{ cm}^{-1}$ in this wavelength range, while in the paper of Taatjes and Oh²⁴ the line strength of one line at 6625.8 cm^{-1} was given as $S = 2.4 \times 10^{-21} \text{ cm}^2 \text{ molecule}^{-1} \text{ cm}^{-1}$. From our calibration, we deduce for this line $S = 4.2 \times 10^{-21} \text{ cm}^2 \text{ molecule}^{-1} \text{ cm}^{-1}$, which is little less than the value given in our previous work²³ for the same line ($S = (5.2 \pm 1.0) \times 10^{-21} \text{ cm}^2 \text{ molecule}^{-1} \text{ cm}^{-1}$). This decrease is partly due to the use of a lower rate constant for k_1 , but it is also probably due to a much more complete calibration procedure. Johnson et al.⁹ reported many difficulties in calibrating their line strength and mentioned that experiments are in progress to measure more accurately both the line positions and line strength; however,

to our knowledge, the results of these experiments have never been published. The value of Taatjes and Oh²⁴ was given only as a footnote, without details on how this value was obtained, which makes it difficult for us to compare the reliability of the results.

If not an absolute, a very good relative agreement was found for the line strength of the most intense line at 6638.2 cm^{-1} . Very recently, Christensen et al.²¹ reported an absorption cross section of $\sigma_{100 \text{ Torr N}_2} = (4 \pm 2) \times 10^{-20} \text{ cm}^2$, estimated relative to the cross sections reported by Johnson et al.⁹ For comparison with our data, we have calculated the absorption cross section under Doppler conditions using an average air-broadening coefficient³⁷ of $\gamma_{\text{coll}} = 0.0115 \text{ cm}^{-1} \text{ atm}^{-1}$ ($\sigma_{\text{Doppler}} = 1.1 \times 10^{-19} \text{ cm}^2$), which is 2.6 times larger than the average of the 23 absorption cross sections reported by Johnson et al.⁹ This is in excellent agreement with the ratio found in this work: $\sigma_{50 \text{ Torr He}} = 2.72 \times 10^{-19} \text{ cm}^2$ (which yields $\sigma_{\text{Doppler}} = 4.2 \times 10^{-19} \text{ cm}^2$), that is, 2.5 times larger than the average of the absorption cross sections of the 24 lines measured in this work in the wavelength range covered by Johnson et al.⁹ (see Figure 1).

It has to be kept in mind that the absorption cross sections given in Table 3 are determined at a total pressure of 50 Torr He. Helium having moderate collision efficiency, the given absorption coefficients can probably be converted for most lines to other He pressures using $\gamma_{\text{coll}} = 0.057 \text{ cm}^{-1} \text{ atm}^{-1}$, independent of the rotational quantum number. Attention should be paid for those lines exhibiting a strong deviation from the average line width of $0.022 \pm 0.005 \text{ cm}^{-1}$ full width at half-maximum (FWHM), as these absorption features are likely to represent several convoluted lines and their broadening behavior might be complex. Working in other bath gases such as N_2 will decrease the absorption cross section: changing, for example, from 50 Torr He to 50 Torr N_2 can decrease the absorption cross section by up to 40%.³⁷

The uncertainties on the reported absorption coefficients have two different origins: the main uncertainty is directly connected to the uncertainty in the rate constant k_1 , as the extracted absorption cross section is directly linked to it. Any future change (increase or decrease) in the recommendation of k_1 can be directly taken into account as it would change (increase or decrease) all absorption cross sections in a proportional manner. In the latest IUPAC recommendation,³⁵ the uncertainty for this rate constant at 298 K is estimated to $\pm 40\%$. However, we find good agreement between our estimated initial HO_2 concentrations, obtained from calculating the photolytic Cl atom concentration, and the one obtained from the intercept of Figure 4- and 5-type plots, using the appropriate absorption cross section.

The other source of uncertainty is linked to the experiment itself: acquiring the entire absorption spectrum took ~ 2 weeks, and our calibration procedure requires that we consider the HO_2 concentration to be constant over the entire period. The photolysis laser was run in constant energy mode, all flows were controlled by calibrated flowmeters, and the total pressure was kept constant and was monitored continuously. We are thus confident that the HO_2 concentration was stable to better than 10%. The calibration procedure is afflicted by uncertainties from (a) the linear regression of individual HO_2 profiles (Figure 4- and 5-type, $< 3\%$ (2σ)), (b) the extrapolation to $[\text{HO}_2]_{0 \rightarrow \infty}$ (Figure 6-type, $< 5\%$ (2σ)), (c) the linear regression of the calibration line (Figure 10, 3% (2σ)), and (d) the fit to the individual lines by a Voigt profile (Figure 9). The global uncertainty linked to the experiment, that is, excluding the

TABLE 3: Top 100 Strongest HO₂ Absorption Lines between 6604 and 6696 cm⁻¹ with Peak Absorption Cross Sections and Line Widths in 50 Torr He^a

ν (cm ⁻¹)	σ (10 ⁻¹⁹ cm ²)	FWHM (cm ⁻¹)	ν (cm ⁻¹)	σ (10 ⁻¹⁹ cm ²)	FWHM (cm ⁻¹)	ν (cm ⁻¹)	σ (10 ⁻¹⁹ cm ²)	FWHM (cm ⁻¹)
6609.45	0.82	0.020	6632.42	1.45	0.027	6664.15	1.29	0.024
6614.42	0.99	0.036	6633.69	1.52	0.023	6666.28	1.63	0.029
6616.36	0.90	0.020	6634.13	0.82	0.018	6666.64	0.82	0.020
6616.77	1.02	0.038	6634.31	1.28	0.025	6668.37	1.32	0.022
6619.08	1.07	0.040	6634.47	0.97	0.024	6668.94	1.09	0.020
6619.67	0.80	0.019	6634.55	0.80	0.019	6669.11	0.80	0.019
6620.91	0.81	0.023	6634.63	1.30	0.025	6669.14	0.82	0.020
6621.34	1.19	0.032	6635.91	1.40	0.023	6669.45	0.79	0.019
6622.15	0.94	0.020	6636.53	1.26	0.022	6669.71	0.84	0.018
6622.89	0.88	0.035	6636.80	1.40	0.044	6670.44	1.45	0.021
6623.32	0.97	0.022	6638.11	1.38	0.023	6670.61	1.29	0.029
6623.57	1.30	0.030	6638.20	2.72	0.023	6671.47	0.85	0.022
6623.73	0.84	0.031	6638.72	0.94	0.016	6672.47	1.55	0.024
6624.56	1.01	0.025	6640.30	1.15	0.021	6672.57	0.82	0.020
6625.02	0.81	0.022	6642.49	0.93	0.020	6673.53	1.40	0.023
6625.27	1.01	0.019	6653.70	0.89	0.022	6674.42	1.39	0.027
6625.66	1.07	0.019	6655.96	0.92	0.021	6674.45	1.70	0.021
6625.78	1.68	0.024	6656.43	0.95	0.022	6677.84	0.99	0.021
6626.28	0.87	0.019	6657.70	0.80	0.022	6678.19	1.37	0.022
6626.90	1.19	0.018	6658.19	0.81	0.024	6679.92	1.63	0.026
6627.58	1.22	0.022	6658.56	0.92	0.022	6681.54	0.99	0.020
6627.99	1.12	0.073	6659.61	0.84	0.021	6683.04	0.83	0.019
6628.86	0.80	0.020	6659.86	1.02	0.021	6683.28	0.84	0.026
6629.20	1.10	0.039	6659.98	0.85	0.020	6683.34	0.83	0.042
6629.85	1.33	0.020	6660.44	1.29	0.027	6683.49	1.04	0.024
6629.89	0.79	0.022	6660.70	1.38	0.025	6684.75	0.85	0.025
6630.15	1.29	0.027	6662.01	1.27	0.022	6688.63	0.81	0.019
6630.21	1.28	0.025	6662.11	0.79	0.020	6691.79	0.92	0.031
6630.36	0.87	0.020	6662.43	0.84	0.021	6693.20	0.83	0.020
6630.76	1.35	0.024	6662.52	1.00	0.018	6693.38	0.82	0.029
6631.09	0.84	0.022	6662.82	0.88	0.021	6693.45	0.83	0.028
6632.09	1.47	0.021	6662.84	0.80	0.020	6695.02	1.02	0.018
6632.32	1.07	0.022	6663.00	0.91	0.018	6695.18	1.02	0.020
6632.35	0.91	0.022						

^a All line positions, except those marked in bold, match a line position assigned by DeSain et al.⁶ by less than 0.01 cm⁻¹.

uncertainty in the rate constant, is estimated to be $\pm 10\%$ for the absorption coefficients of the eight lines in Table 2 (only afflicted by type (a) and (b) uncertainties), while it is estimated to be $\pm 25\%$ for all other lines from Table 3 (impacted also by (c)- and (d)-type uncertainties).

The line positions were anchored to the line positions given by DeSain et al.;⁶ the line positions of 81 out of the 100 lines in Table 3 were found to match to better than 0.01 cm⁻¹ with a transition assigned by DeSain et al., with the average deviation being 0.0027 cm⁻¹. We thus estimate the line positions given in Table 3 to be accurate to better than 0.01 cm⁻¹.

A single shot detection limit ($S/N = 1$) for our actual setup (mirrors with $R = 0.99996$ with $\tau_0 = 40 \mu\text{s}$) of $[\text{HO}_2] = 6.5 \times 10^{10} \text{ cm}^{-3}$ can be calculated for the most intense absorption line at 6638.20 cm⁻¹ ($\sigma = 2.72 \times 10^{-19} \text{ cm}^2$ at 50 Torr), assuming a measurable decrease in the ring-down time of 0.4 μs . Reducing the pressure and averaging can easily decrease this detection limit by a factor of 2.

Conclusion

We have measured the absorption spectrum of the 2ν₁ band of HO₂ radicals in the wavelength range 6604–6696 cm⁻¹ by cw-CRDS coupled to laser photolysis. The absorption coefficients were converted to absolute absorption cross sections by deducing the initial radical concentration from kinetic decays. The strongest line was observed at 6638.20 cm⁻¹, nearly a factor of 2 stronger than the second-strongest line observed in this wavelength range. The absorption cross section for this line in 50 Torr He was determined to be $\sigma = 2.72 \times 10^{-19} \text{ cm}^2$.

Acknowledgment. The work has been financially supported by the Région Nord/Pas de Calais within the framework of IRENI, by the CNRS, by the European funds for Regional Economic Development FEDER, and by the French National Programme “Les Enveloppes Fluides” (LEFE)–“Chimie Atmosphérique” (CHAT). The authors are grateful to Pascal Szriftgiser for lending his Agilent laser module for several weeks.

Supporting Information Available: Entire absorption spectrum of the HO₂ radical. This material is available free of charge via the Internet at <http://pubs.acs.org>.

References and Notes

- (1) Ludwig, W.; Brandt, B.; Friedrichs, G.; Temps, F. *J. Phys. Chem. A* **2006**, *110*, 3330–3337.
- (2) Anglada, J. M.; Olivella, S.; Sole, A. *J. Phys. Chem. A* **2006**, *110*, 6073–6082.
- (3) Christensen, L. E.; Okumura, M.; Hansen, J. C.; Sander, S. P.; Francisco, J. S. *J. Phys. Chem. A* **2006**, *110*, 6948–6959.
- (4) Suzuki, K.; Kanno, N.; Tonokura, K.; Koshi, M.; Tsuchiya, K.; Tezaki, A. *Chem. Phys. Lett.* **2006**, *425*, 179–184.
- (5) Christensen, L. E.; Okumura, M.; Sander, S. P.; Salawitch, R. J.; Toon, G. C.; Sen, B.; Blavier, J. F.; Jucks, K. W. *Geophys. Res. Lett.* **2002**, *29*, 1299.
- (6) DeSain, J. D.; Hob, A. D.; Taatjes, C. A. *J. Mol. Spectrosc.* **2003**, *219*, 163–169.
- (7) Fink, E. H.; Ramsay, D. A. *J. Mol. Spectrosc.* **1997**, *185*, 304–324.
- (8) Crowley, J. N.; Simon, F. G.; Burrows, J. P.; Moortgat, G. K.; Jenkin, M. E.; Cox, R. A. *J. Photochem. Photobiol., A* **1991**, *60*, 1–10.
- (9) Johnson, T. J.; Wienhold, F. G.; Burrows, J. P.; Harris, G. W.; Burkhard, H. *J. Phys. Chem.* **1991**, *95*, 6499–6502.

- (10) Nelson, D. D., Jr.; Zahniser, M. S. *J. Mol. Spectrosc.* **1991**, *150*, 527–534.
- (11) Fink, E. H.; Ramsay, D. A. *J. Mol. Spectrosc.* **2002**, *216*, 322–334.
- (12) Kanno, N.; Tonokura, K.; Tezaki, A.; Koshi, M. *J. Phys. Chem. A* **2005**, *109*, 3153–3158.
- (13) Stone, D.; Rowley, D. M. *Phys. Chem. Chem. Phys.* **2005**, *7*, 2156–2163.
- (14) Jemi-Alade, A. A.; Lightfoot, P. D.; Lesclaux, R. *Chem. Phys. Lett.* **1992**, *195*, 25–30.
- (15) Tomas, A.; Villenave, E.; Lesclaux, R. *J. Phys. Chem. A* **2001**, *105*, 3505–3514.
- (16) Jenkin, M. E.; Cox, R. A.; Hayman, G. D.; Whyte, L. J. *J. Chem. Soc., Faraday Trans. 2* **1988**, *84*, 913–930.
- (17) Nielsen, O. J.; Johnson, M. S.; Wallington, T. J.; Christensen, L. K.; Platz, J. *Int. J. Chem. Kinet.* **2002**, *34*, 283–291.
- (18) Becker, K. H.; Fink, E. H.; Langen, P.; Schurath, U. *J. Chem. Phys.* **1974**, *60*, 4623–4625.
- (19) Hunziker, H. E.; Wendt, H. R. *J. Chem. Phys.* **1974**, *60*, 4622–4623.
- (20) Zahniser, M. S.; Stanton, A. C. *J. Chem. Phys.* **1984**, *80*, 4951–4960.
- (21) Christensen, L. E.; Okumura, M.; Sander, S. P.; Friedl, R. R.; Miller, C. E.; Sloan, J. J. *J. Phys. Chem. A* **2004**, *108*, 80–91.
- (22) Kanno, N.; Tonokura, K.; Tezaki, A.; Koshi, M. *J. Mol. Spectrosc.* **2005**, *229*, 193–197.
- (23) Thiebaud, J.; Fittschen, C. *Appl. Phys. B: Lasers Opt.* **2006**, *85*, 383–389.
- (24) Taatjes, C. A.; Oh, D. B. *Appl. Opt.* **1997**, *36*, 5817–5821.
- (25) Chichinin, A.; Einfeld, T. S.; Gericke, K. H.; Grunenberg, J.; Maul, C.; Schäfer, L. V. *Phys. Chem. Chem. Phys.* **2005**, *7*, 301–309.
- (26) Sehested, J.; Mögelberg, T.; Fägerström, K.; Mahmoud, G.; Wallington, T. J. *Int. J. Chem. Kinet.* **1997**, *29*, 673–682.
- (27) Maricq, M. M.; Szente, J. J. *J. Phys. Chem.* **1994**, *98*, 2078–2082.
- (28) Kurylo, M. J.; Ouellette, P. A.; Laufer, A. H. *J. Phys. Chem.* **1986**, *90*, 437–440.
- (29) Cox, R. A.; Burrows, J. P. *J. Phys. Chem.* **1979**, *83*, 2560–2568.
- (30) Andersson, B. Y.; Cox, R. A.; Jenkin, M. E. *Int. J. Chem. Kinet.* **1988**, *20*, 283–295.
- (31) Zhu, R. S.; Lin, M. C. *Chem. Phys. Lett.* **2002**, *354*, 217–226.
- (32) Zhu, R. S.; Lin, M. C. *PhysChemComm* **2001**, *4*, 106–111.
- (33) Lii, R.-R., Jr.; Sauer, M. C.; Gordon, S. J. *J. Phys. Chem.* **1981**, *85*, 2833–2834.
- (34) Hamilton, E. J.; Lii, R.-R. *Int. J. Chem. Kinet.* **1977**, *9*, 875–885.
- (35) Atkinson, R.; Baulch, D. L.; Cox, R. A.; Crowley, J. N.; Hampson, R. F., Jr.; Hynes, R. F.; Jenkin, R. G.; Rossi, M. J.; Troe, J. *Atmos. Chem. Phys.* **2004**, *4*, 1461–1738.
- (36) Sander, S. P.; Kurylo, M. J.; Orkin, V. L.; Golden, D. M.; Huie, R. E.; Finlayson-Pitts, B. J.; Kolb, C. E.; Molina, M. J.; Friedl, R. R.; Ravishankara, A. R.; Moortgat, G. K. *JPL Publ.* **2003**, 02-25.
- (37) Ibrahim, N.; Thiebaud, J.; Orphal, J.; Fittschen, C. *J. Mol. Spectrosc.* **2007**, *242*, 64–69.